Fundamental Research 5 (2025) 138–144

Contents lists available at ScienceDirect

Fundamental Research

journal homepage: http://www.keaipublishing.com/en/journals/fundamental-research/

Article

Flat-band based high-temperature ferromagnetic semiconducting state in the graphitic C_4N_3 monolayer

Chaoyu He [a], Yujie Liao [a], Tao Ouyang [a,*], Huimin Zhang [b,*], Hongjun Xiang [b,*], Jianxin Zhong [a]

[a] Laboratory for Quantum Engineering and Micro-Nano Energy Technology and School of Physics and Optoelectronics, Xiangtan University, Xiangtan 411105, China
[b] Key Laboratory of Computational Physical Sciences (Ministry of Education), Institute of Computational Physical Sciences, Department of Physics, Fudan University, Shanghai 200433, China

ARTICLE INFO

Article history:
Received 31 January 2023
Received in revised form 19 November 2023
Accepted 12 December 2023
Available online 17 December 2023

Keywords:
Graphitic C_4N_3
Isolated flat-band
Ferromagnetic semiconductor
Two-dimensional multiferroic
First-principles calculation
Tight-binding model

ABSTRACT

Half-filled isolated flat-band paves a new way to realize high-temperature ferromagnetic semiconductor for spintronics applications, but it is extremely rare in lattice models and lacking in realistic materials. Herein, the 2×2 super-cell of the honeycomb lattice with a single-hole defect is proposed as a new lattice model (HL-D-1/8) to realize nontrivial isolated flat-bands. We further demonstrate that C_4N_3 monolayer of the experimentally realized graphitic carbon nitride (Adv. Mater., 22, 1004, 2010; Nat. Commun., 9, 3366, 2018) is a perfect system holding such a lattice to host flat-bands. A new corrugated Pca21 configuration is proposed as the ground state for the free-standing C_4N_3 monolayer, which is dynamically stable and energetically more favorable than the widely-used flat one without dynamical stability. The Pca21 configuration is found to be an intrinsic ferromagnetic half-semiconductor ($T_c \approx 241$ K) with one semiconducting spin-channel (1.75 eV) and one insulating spin-channel (3.64 eV), which is quite rare in two-dimensional systems. Its ferromagnetic semiconducting property originates from the isolated p_z-state flat-band as the corrugation shifts the flat-band upward to the Fermi level. Interestingly, such a corrugated Pca21 C_4N_3 monolayer is found to be both piezoelectric and ferroelectric, which makes it an unusual metal-free two-dimensional multiferroic.

1. Introduction

The bands near the Fermi level dominate the physical properties of condensed materials. Two limiting cases classified according to effective mass of carriers have attracted widely research interests, namely, the linearly dispersed band [1] and the flat-band [2–4] holding massless Dirac fermion and infinitely heavy fermion, respectively. The linearly dispersed band has been experimentally detected in graphene monolayer [1] and the flat-band can be realized in the moire superlattice based on graphene bilayer [5,6]. In fact, flat-band has been widely investigated in different lattice models [2-4,7-9] in the past decades and also be theoretically predicted in many stoichiometric materials [2-4,10-13]. Exotic quantum phases, such as high temperature fractional quantum Hall effects [14], Bose-Einstein condensation [15], Wigner crystallization [16,17], high-temperature superconductivity [18] and ferromagnetism [12,19], are verified to exist in flat-band systems. However, the definite experimental observations of electronic flat-band in two-dimensional (2*D*) stoichiometric systems are still quite rare [2–4], which seriously hinders the realization of these exotic quantum states.

Recently, 2*D* ferromagnetic (FM) semiconductors, such as CrX_3 (X=Cl, Br, I) [20,21], VI_3 [22], $CrGeTe_3$ [23] and CrSBr [24] attracted much attention as they are potential material-basis for nano-scale spin-electronics [25,26], e.g., single-spin transistor [27], magnetic tunnel junctions [28] and other spin-dependent devices [29,30]. The half-filled isolated flat-bands usually induce ferromagnetism due to Hubbard repulsion [31,32], which provides new possibilities to design potential 2D FM semiconductors with high Curie temperature. However, the isolated flat-band near the Fermi-level is extremely rare in both lattice models [9,33,34] and material platforms [35,36]. Most of the previously proposed flat-bands are full-filled and they always touch together with a dispersive band with a wide band width larger than the spin-split energy, which prevents the formation of FM semiconductor [11-13,17]. That is to say, the intrinsic half-filled and isolated flat-bands in realistic materials are still lacking for realizing the stable semiconducting FM orders.

In this work, a simple lattice-model is proposed through introducing single-hole defect in the hexagonal 2×2 super-cell of the well-known honeycomb lattice (HL-D-1/8) for designing isolated flat-band with tight-binding method (TB). The HL-D-1/8 holds one isolated zero-energy flat-band and two groups of the Kagome-type flat-bands. We demonstrate that these nontrivial flat-bands can be realized in a HL-D-1/8 related C_4N_3 monolayer [37–43] which is the single layer of the

* Corresponding authors.
E-mail addresses: ouyangtao@xtu.edu.cn (T. Ouyang), hmzhang@fudan.edu.cn (H. Zhang), hxiang@fudan.edu.cn (H. Xiang).

https://doi.org/10.1016/j.fmre.2023.12.001

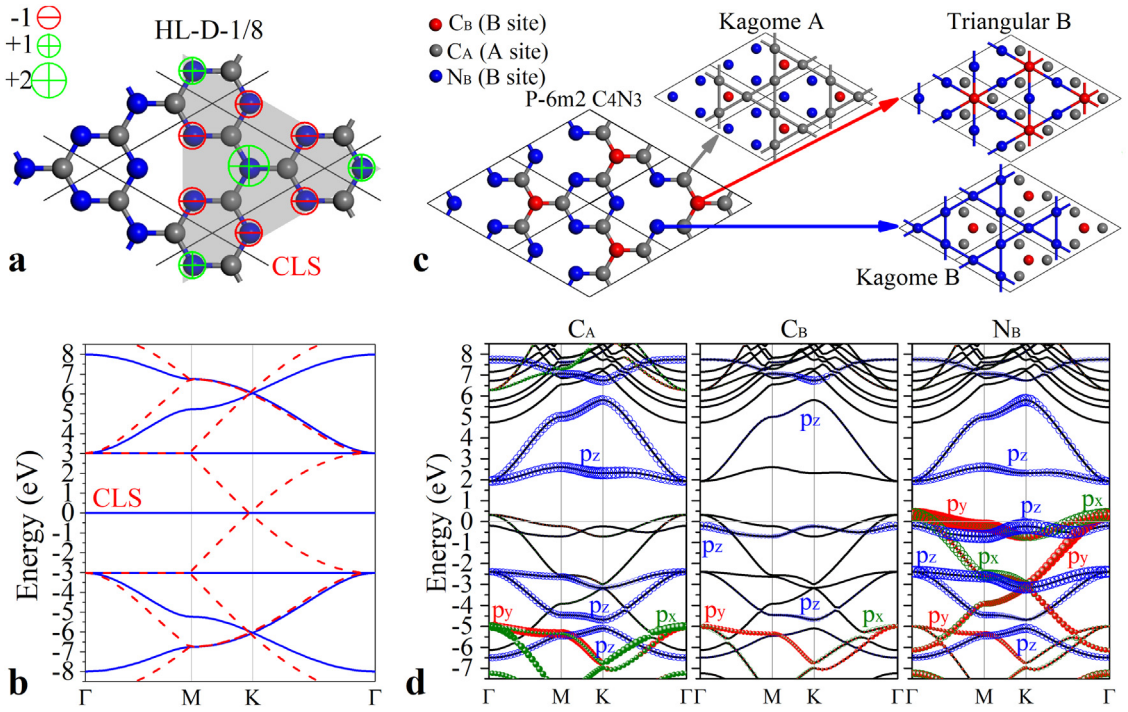

Fig. 1. Flat-band Lattice and Material. (a) The hexagonal 2 × 2 super-cell of the well-known honeycomb lattice (HL) with single-hole defect (HL-D-1/8), where grey and blue balls indicate A and B sublattices, respectively. For the compact localized states (CLS), the values of the basis-wave-function amplitudes at different sites are +2, +1 and −1, respectively. (b) The corresponding p_z-wave band structures for the 2 × 2 super-cell with (red dash lines) and without single-hole defect (blue solid lines). (c) The crystal structure of the flat P-6m2 C_4N_3 monolayer and its three inequivalent sublattices of Kagome A, Kagome B and Triangular B filled with carbon, nitrogen and carbon atoms, respectively. (d) The projected p-state waves (p_x, p_y *and* p_z orbitals) of different C_A, C_B and N_B atoms in the calculated band structure in NM state of the flat P-6m2 C_4N_3 monolayer.

experimentally synthesized graphitic carbon nitride [44,45]. Furthermore, possible corrugations in free-standing C_4N_3 monolayers are systematically generated by a random method based on group and graph theory (RG2) [46,47] and investigated through the first-principles calculations. For free-standing C_4N_3 monolayer, its ground state is identified to be a highly corrugated Pca21 configuration with positive dynamical stability and remarkable energetic stability exceeding than the widely-used flat one. Our first principles calculations show that Pca21 C_4N_3 monolayer is a FM semiconductor, which is quite rare in 2D materials family. The physical mechanism of the magnetism origin can be well understood by the split effects of spin-exchange and crystal-field. Moreover, the graphitic C_4N_3 monolayer is further verified to be an unusual metal-free 2D multiferroic with FM semiconducting, ferroelectric and piezoelectric properties for information application.

2. A new flat-band model and its realization

In this section, we will first introduce a new TB lattice model that hosts the isolated flat-bands. Then we show that this flat-band model can be realized in an experimentally synthesized material, i.e., graphitic C_4N_3 [44,45]. As shown in Fig. 1a, the proposed lattice model is named as HL-D-1/8 which is constructed with the 2 × 2 super-cell of the well-known honeycomb lattice (HL) through introducing a single-hole defect (1/8 means the defect density). In the perfect 2 × 2 super-cell of honeycomb lattice, A and B sublattices share the same on-site energy and the adjacent hopping integrals between them are also equal to each other. It contains two dispersive p_z-wave bands with $E_1(\mathbf{k}) = -E_2(\mathbf{k})$ for any $\mathbf{k}$ vector due to the chiral (sublattice) symmetry of $SH(\mathbf{k})S^{-1} = -H(\mathbf{k})$, where S is the Pauli matrix of σ_3. These two bands degenerate at the high-symmetry **K** point of (1/3, 1/3, 0) forming a Dirac-cone due to the C_3 symmetry of this k-vector, as shown in Fig. 1b in the band structure with red dash lines. The introduced single-hole defect (deleting one A site) does not broke the chiral symmetry of the super-cell and will introduce an exactly half-filled zero energy flat-band on the Fermi-level due to the odd number (2N-1) of lattice sites. The corresponding band structure for HL-D-1/8 is shown in Fig. 1b in blue solid lines. Since the two-fold degenerating Dirac-cones at K and K' are not folded to the same k-point in 2 × 2 super-cell, they will be broken by the introduced single-hole defect so that the corresponding zero energy flat-band becomes isolated. Such a zero-energy flat-band can also be understood by the destructive interference between the compact localized states (CLS) in HL-D-1/8 as indicated in Fig. 1a. And it must localize in the majority sublattice that is named the B sublattice in HL-D-1/8, which is similar to the case as discussed previously in the defected graphene monolayer [36].

As shown in Fig. 1c, the HL-D-1/8 contains three sublattices: one triangular sublattice and two Kagome sublattices. Each site of the triangular sublattice and one (Kagome A) of the Kagome sublattices are three-fold coordinated, while the sites in the Kagome A sublattice are two-fold coordinated. To realize HL-D-1/8 in a realistic material, we notice that elements C and N are reasonable selections because they prefer 3-coordinated sp^2-hybridization and 2-coordinated sp^3-hybridization in 2D case, respectively. Thus, we occupy 3 C atoms in Kagome A (C_A), 1 C atom in triangular B (C_B) and 3 N atoms in Kagome B (N_B), to construct a C_4N_3 monolayer for realizing the nontrivial flat-bands in HL-D-1/8. We note that the graphitic C_3N_4 material was synthesized experimentally [44,45]. As shown in Fig. 1d, the electronic band structures of such a HL-D-1/8 related C_4N_3 (P-6m2) are calculated by first-principles method, in which the long-range interactions, site differences (on-site energies) as well as the p_x and p_y orbitals are naturally included. The p_z-orbitals of C_A, C_B and N_B atoms in different sublattices are projected in the calculated band structures, respectively. It clearly shows that these projected p_z-states in the flat P-6m2 C_4N_3 monolayer are very similar to the p_z-based TB band structure of HL-D-1/8 as shown in Fig. 1b. However, with

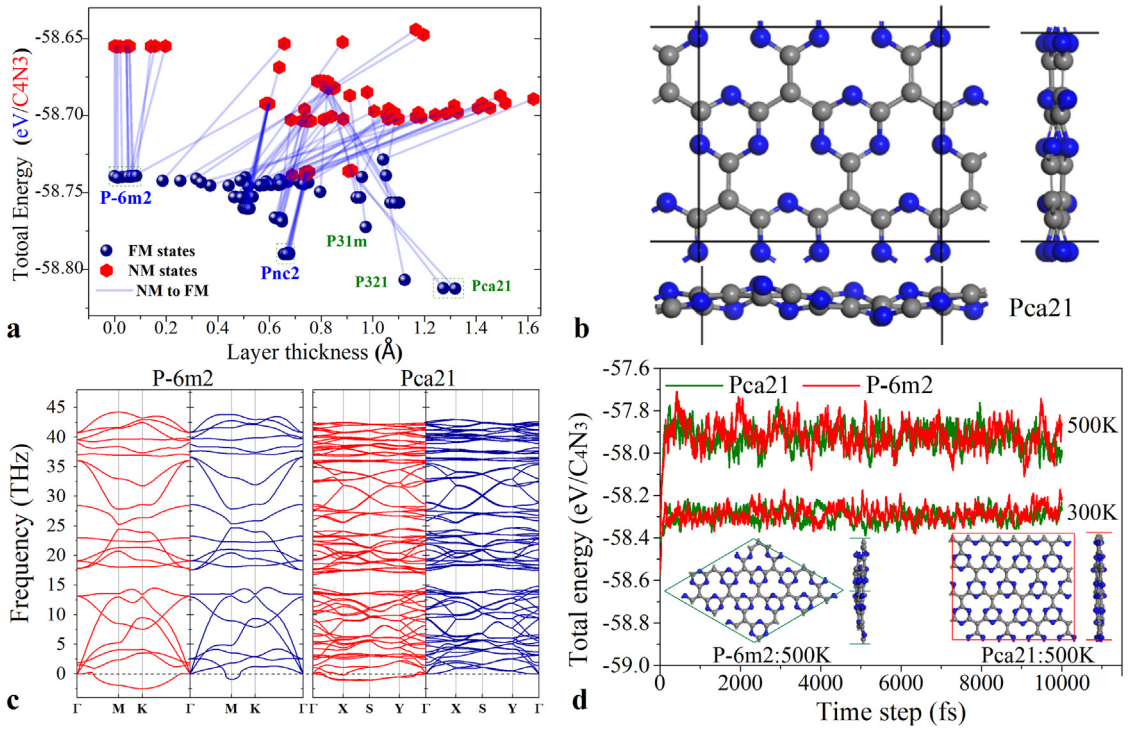

Fig. 2. Structures and stabilities. (a) The total energies of different corrugations (including flat P-6m2, previously proposed Pnc2 and the new Pca21) in NM and FM states. (b) The optimized crystalline structures of the new ground state Pca21 in different top and side views.(c) The simulated vibrational spectrums for the flat P-6m2 and the corrugated Pca21 in both NM (red solid lines) and FM (blue solid lines) situations. (d) The fluctuations of the total energy of the flat P-6m2 (red solid line) and corrugated Pca21 (green solid line) C_4N_3 monolayers in 300 K and 500 K AIMD, as well as the corresponding structural snapshots selected from the process in 500 K.

long-range interactions in first-principles calculations, the "zero-energy flat-band" is obviously distorted and it is always buried by the p_x and p_y states contributed from the N atoms in the Kagome B sublattice. Whereas these p_x and p_y states from N atoms contribute new Kagome-type flat-bands nearby the Fermi-level. Importantly, the Kagome-type flat-bands are partially-filled, which introduces magnetism in the flat P-6m2 C_4N_3 monolayer to make it to be a FM half-metal that is also reported in previous study [44]. The flat P-6m2 C_4N_3 has been taken [44,45] as a single layer of the experimentally synthesized graphitic carbon nitride [44,45]. However, its FM half-meallic property is inconsistent with the experimentally reported semiconducting feature [44,45], suggesting that we need to search for new structure candidate for the experimentally synthesized graphitic carbon nitride.

3. New ground state structure of monolayer C_4N_3

In 2012, a slightly corrugated Pnc2 configuration [39,44] with a lower energy was proposed as a new candidate of the experimentally synthesized graphitic C_4N_3. However, such a slightly-corrugated Pnc2 configuration is still FM half-metallic, which disagrees with the experimental observation. For graphitic C_3N_4 monolayer, a new highly corrugated configuration (Pca21) has been confirmed to be its ground state [48], which is more stable than the slightly corrugated Pnc2 one. Up to now, there is no systematic work on investigating the structures and stabilities of possible corrugations for C_4N_3 monolayer in its free-standing case and this becomes an important part of our research work. Based on the super-cells of the flat P-6m2 as shown in Fig. S1 (a), 98 possible corrugations (including the previously proposed Pnc2 [39]) are generated by RG2 code [46,47]. These corrugated configurations are systematically optimized by the widely used VASP [49] code in both FM and NM states. Here, only FM and NM states are considered to optimize the structures because that we have checked some possible antiferromagnetic configurations for the flat P-6m2, the slightly corrugated Pnc2 as well as the highly corrugated Pca21 and confirmed that FM is always the ground magnetic state. As the total energies plotted in Fig. 2a as a function of the layer-thicknesses, most of the corrugated candidates are more favorable than the flat P-6m2 one and the FM states are always more stable than the NM states in any configurations. The corrugation induced energy release in these systems can be qualitatively understood by the reduced coulomb repulsion energy between surface charges due to the enlarged space for charge redistribution. Particularly, we find a new structural candidate (Pca21) with outstanding energetic stability exceeding than the flat P-6m2 and the previously proposed Pnc2 reconstruction as its crystalline structure shown in Fig. 2b. Its largest layer-thickness makes it the most stable one among all the discovered corrugations. The details of the structural relations between the flat P-6m2, the previously proposed Pnc2, as well as the new discovered low-energy P321 and Pca21 are discussed in the supplementary file in Fig. S1b.

Low-energy means high probability of the existence in natural or experimental conditions if the phase is both dynamically and mechanically stable against small lattice vibration and deformation. The simulated vibrational spectrums of the flat P-6m2 as well as the corrugated Pca21 in both FM and NM states are shown in Fig. 2c. It is clear that the flat P-6m2 one is dynamically unstable in both FM and NM situations, while the corrugated Pca21 is dynamically stable in FM state but unstable in NM situation. The results in Fig. 2d show that the atomic configuration of Pca21 remains intact with only small deformations and the total energy just oscillates within a very narrow range in both 300 K and 500 K AIMD simulation, implying that Pca21 is thermally stable. However, the atomic configuration of P-6m2 is obviously corrugated under the AIMD simulation although its total energy oscillates is also in a very narrow range, which means that the free-standing graphitic C_4N_3 monolayer prefers the corrugated configuration more than the exactly flat one. In addition, the calculated elastic constants C_{11}, C_{12},

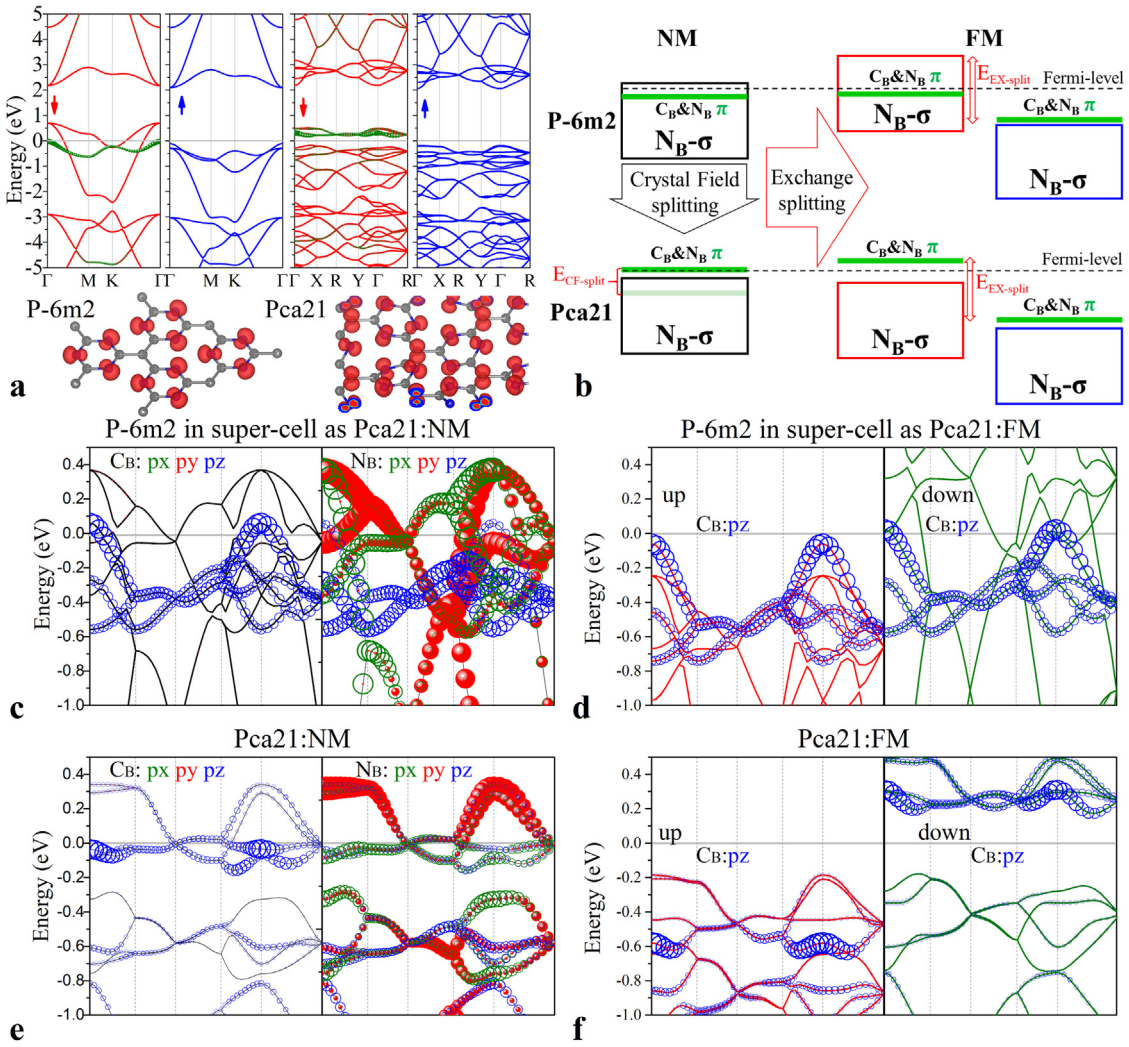

Fig. 3. Magnetism and its mechanism. (a) The FM-state band structures with projected p_z states (Olive solid balls) of the carbon atoms C_B together with corresponding spin-charge densities for the flat P-6m2 and the corrugated ground state Pca21. (b) The orbital evolutions from flat P-6m2 to corrugated Pca21 in both NM and FM states for showing split-effects of crystal-field ($E_{CF-split}$) and spin-exchange ($E_{EX-split}$) to explain the origin of FM semiconducting property.(c)-(f) The projected band structures for showing the true evolutions of the p_x, p_y and p_z bands from N_B atoms, as well as the isolated p_z-state flat-band from the C_B atoms in the flat P-6m2 and the corrugated Pca21.

C_{22} and C_{66} for the corrugated Pca21 are 124.79 N/m, −20.38 N/m, 84.10 N/m and 70.37 N/m, respectively, which suggests that Pca21 is also mechanically stable to resist small-deformations according to the mechanical stability criteria ($C_{11} \times C_{22} - C_{12}^2 > 0, C_{66} > 0$) for 2D materials.

4. Electronic and magnetic properties of C_4N_3

The flat P-6m2 C_4N_3 monolayer is a FM half-metal [44] as its band structure shown in Fig. 3a. As reported in previous literature [39], slight corrugation in Pnc2 configuration does not affect such a half-metallic property (as the band structure shown in Fig. S2). However, the highly-corrugated Pca21 is a FM semiconductor as its band structure depicted in Fig. 3a, which is quite rare in 2D materials. Such an exciting property can be confirmed by the high-level HSE06 method as shown in Fig. S3. In fact, Pca21 configuration is a FM half-semiconductor holding one semiconducting channel with band gap of 1.75 eV and one insulating channel with larger band gap of 3.64 eV. The FM semiconducting property can be understood by the synergistic effect between spin-split and crystal-field split as the schematic picture shown in Fig. 3b. Here, only the p_z orbitals of C_B and N_B atoms (π band), as well as the p_x and p_y orbitals (σ bands) of N_B atoms near the Fermi-level are considered to show the split-effects of crystal-field and spin-exchange. The true evolutions can be noticed in Fig. 3c-f, where the p_x, p_y and p_z bands from N_B, as well as the isolated p_z-state flat-band from the C_B in Pca21 and P-6m2 (with compatible super-cell) are plotted together in both NM and FM states.

For the flat P-6m2 configuration, the magnetism originates from the spin-split effect induced by its partially-filled Kagome-type (σ bands from N_B atoms) flat-band and the metallic feature is maintained due to the wide dispersion-range of the Kagome-type linear band. We notice that the isolated flat π band (p_z-state) from C_B atoms is always full-filled in both NM and FM situations. With further enlarged the crystal-field splitting ($E_{CF-split}$) effect due to corrugation, the π band in Pca21 will be higher so that it becomes isolated from the wide N-σ bands with an obvious band gap of about 0.2 eV under the fixed magnetic state of FM. This is because the corrugation weakens the electrostatic repulsion between the σ electrons in N_B atoms. As shown in Fig. 3e, the true π bands from C_B and N_B atoms in Pca21 form a narrow group locating in the energy-range of about 0.42 eV and it is half-filled. When the degree of spin is considered, such a narrow group will further split into two sub-groups of spin-up and spin-down (Fig. 3f). Considering that the average split energy ($E_{EX-split}$) in Pca21 is obviously larger than the width of the narrow group, the sub-group of spin-up is exactly full-filled and

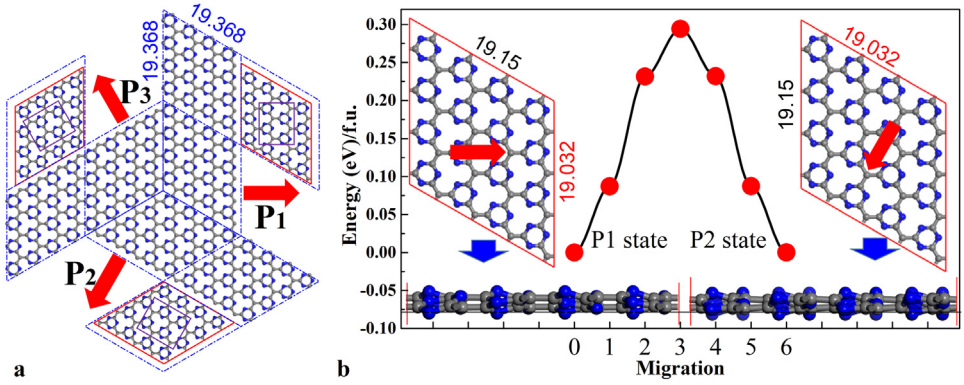

Fig. 4. Ferroelectricity and path ways. (a) Plotted are the three possible corrugation path ways from the flat P-6m2 (in blue dash 4 × 4 super-cells) to the corrugated Pca21 (in red solid super-cells and violet primetive cells). (b)The NEB pathway and barrier from polarized P_1 state to P_2 state and the corresponding configurations.

the spin-down sub-group is totally unoccupied. Accordingly, the corrugated Pca21 becomes semiconductor under FM situation due to the synergistic effect of crystal-field and spin-exchange. Thus, the narrow band-groups with inter-groups' gaps induced by corrugations are critical for forming the FM semiconducting properties in Pca21. These isolated narrow band-groups play the roles of the isolated flat-bands that have been considered as physical mechanism for FM semiconducting properties in previous literatures [50,51]. Corrugation induced opening of the inter-groups' gaps and the correspondingly enhanced spin-split effects as the gradually increased layer-thickness can be noticed from the corresponding band structures as shown in Fig. S4.

The semiconducting property and the absence of inversion symmetry in C_{2v} indicate that the corrugated Pca21 is a potential material with both piezoelectric and ferroelectric properties. It is interesting that there are three equivalent transition pathways from the flat P-6m2 to the corrugated Pca21 as shown in Fig. 4a and exist corresponding three equivalent ferroelectric phases (P1, P2 and P3) with in-plane spontaneous polarizations along three different directions. These three polarization directions form about 120° angles with each other, which is different from the traditional case of two antiparallel polarization directions (180°). Using the standard Berry phase method [52], the polarization in Pca21 C_4N_3 is calculated to be of 7.66×10^{-8} μC/cm, which is equal to 5.86 μC/cm^2 in the three-dimensional situation when considering the monolayer thickness. The polarization is relatively larger than that in the 1T-MoS_2 (0.22 μC/cm^2) [53] and in the van der Waals interlayer-sliding ferroelectric BN (2.08×10^{-8} μC/cm in 2D and ~0.68 μC/cm^2 in 3D) [54]. As shown in Fig. 4b, the migration barrier between the two ferroelectric states is evaluated to be 0.29 eV/f.u. based on the climbing-image nudged elastic band (CI-NEB) method [55]. Furthermore, the two piezoelectric coefficients of d_{11} and d_{12} for the corrugated Pca21 are calculated to be 9.659 pm/V and 5.119 pm/V, respectively, which are even larger than that of MoS_2 monolayer [56].

Additionally, it is interesting to evaluate the Curie temperature in such a metal-free FM semiconductor. Thus, a spin effective Hamiltonian is constructed as $H = \sum_{ij} J_{ij} S_i \cdot S_j$ under the nearest exchange interaction approximate, where $S_i(S_j)$ indicates the spin vector on site i (j) and J_{ij} is the exchange interaction between sites i and j. Since each localized state is centered at the C_B atoms in triangular B sublattice, we regard the C_B atoms as spin sites, while the magnetic moments on N_B atoms are induced by the C_B atoms. Using the DFT-based total energies of two different spin configurations, the nearest spin exchange interactions (J_1) can be deduced through energies mapping. In the C_4N_3 structure with Pca21 symmetry, J_1 is evaluated to be −17.63 meV with setting total effective spin $S = 1$. This negative value of J_1 further indicates that FM is the ground magnetic state for graphitic C_4N_3 monolayer with Pca21 configuration. And the corresponding Curie temperature of Pca21 is estimated to be 241 K based on the Monte Carlo simulation, which is much higher than those of the experimental synthesized 2D FM semiconductors.

5. Discussion

On the one hand, the isolated flat-band causes ferromagnetism in graphitic C_4N_3 because of the corrugation of the structure. On the other hand, as the isolated flat-band shifted upward by crystal-field splitting, there opens a band gap, which would reduce the screening by free carries and realize the ferroelectric polarization. It is worth to be noted that the graphitic C_4N_3 monolayer in corrugated Pca21 configuration is both ferromagnetic and ferroelectric. To our knowledge, it is the first prediction in flat-band family that a material is reported to be multiferroic. This mechanism could supply a new way to design 2D multiferroics in flat-band system and broaden the research scope of flat-band materials. Moreover, our study shows that such a small scale graphitic C_4N_3 monolayer with multiferroicity may have large potential application in the future high-density memories or electronics.

Twisted bilayer graphene (TBG) is one of the most well-known flat-band systems. We now discuss the similarities and differences between TBG and C_4N_3. The emergence of flat-bands in TBG is attributed to the peculiar interlayer hybridization at a magic twisted angle [57] and is related to the flatness of the lowest Landau level in quantum Hall effect on torus [58]. In graphitic C_4N_3 monolayer, the flat-band originates from the chiral (sublattice) symmetry of the lattice as we discussed above. In both cases, the flat-bands are isolated from the other valence and conduction bands. However, the separation between the isolated flat-bands and other bands in the TBG case is very small (i.e., on the order of 10 meV), while it is 200 meV in the non-magnetic case in C_4N_3 and the insulating band gap of the ferromagnetic state is larger than 1 eV from the HSE calculations. The flat-band ferromagnetism in TBG has been predicted [50] and experimentally observed near three-quarters filling [59]. However, the ferromagnetic Curie temperature in TBG is rather low (i.e., ~4 K) and it is suggested that the ferromagnetism is primarily orbital in nature [60]. In the C_4N_3 case, the ferromagnetic Curie temperature is higher than 200 K and the magnetization is mainly due to the spin contribution.

6. Conclusion

This work has proposed a new lattice model (HL-D-1/8) to realize nontrivial flat-bands based on p_z-orbital TB calculations. We demonstrate that such nontrivial flat-bands can be well identified in the DFT-based band structures of graphitic C_4N_3 monolayer, which is structurally isomorphic to HL-D-1/8. As a single layer of the experimentally synthesized graphitic carbon nitride, C_4N_3 monolayer in free-standing case prefers the corrugated Pca21 configuration as its ground state but

not the half-metallic configurations in flat P-6m2 or corrugated Pnc2. Furthermore, the free-standing C_4N_3 monolayer with P-ca21 configuration is carefully confirmed as a flat-band related FM half-semiconductor with one semiconducting spin-channel and one insulating spin-channel, which is quite rare in 2D materials. Its Curie temperature is evaluated to be 241 K, which is much higher than those of the experimental synthesized 2D FM semiconductors. The discoveries in our work highlight that the experimentally realized graphitic C_4N_3 monolayer in free-standing case is an unusual metal-free 2D multiferroic with FM semiconducting, ferroelectric and piezoelectric properties for information application.

Declaration of competing interest

The authors declare that they have no conflicts of interest in this work.

Acknowledgments

This work is supported by the National Natural Science Foundation of China (52372260, 11974300, 11974299 and 12204397), the Science Fund for Distinguished Young Scholars of Hunan Province of China (2021JJ10036) and the Youth Science and Technology Talent Project of Hunan Province (2022RC1197). Work at Fudan is supported by NSFC (11825403, 11991061, and 12188101) and Guangdong Major Project of Basic and Applied Basic Research (Future functional materials under extreme conditions-2021B0301030005). H.-M.Z was supported by the Jiangsu Funding Program for Excellent Postdoctoral Talent.

Supplementary materials

Supplementary material associated with this article can be found, in the online version, at doi:10.1016/j.fmre.2023.12.001.

References

[1] A.C. Neto, F. Guinea, N.M. Peres, et al., The electronic properties of graphene, Rev. Mod. Phys. 81 (1) (2009) 109.
[2] Z. Liu, F. Liu, Y.-S. Wu, Exotic electronic states in the world of flat bands: From theory to material, Chin. Phys. B 23 (7) (2014) 077308.
[3] H. Liu, S. Meng, F. Liu, Screening two-dimensional materials with topological flat bands, Phys. Rev. Mater. 5 (8) (2021) 084203.
[4] N. Regnault, Y. Xu, M.-R. Li, et al., Catalogue of flat-band stoichiometric materials, Nature 603 (7903) (2022) 824–828.
[5] Y. Cao, V. Fatemi, S. Fang, et al., Unconventional superconductivity in magic-angle graphene superlattices, Nature 556 (7699) (2018) 43–50.
[6] Y. Cao, V. Fatemi, A. Demir, et al., Correlated insulator behaviour at half-filling in magic-angle graphene superlattices, Nature 556 (7699) (2018) 80–84.
[7] H. Liu, G. Sethi, S. Meng, et al., Orbital design of flat bands in non-line-graph lattices via line-graph wave functions, Phys. Rev. B 105 (8) (2022) 085128.
[8] C.S. Chiu, A.N. Carroll, N. Regnault, et al., Line-graph-lattice crystal structures of stoichiometric materials, Phys. Rev. Res. 4 (2) (2022) 023063.
[9] D. Călugăru, A. Chew, L. Elcoro, et al., General construction and topological classification of crystalline flat bands, Nat. Phys. 18 (2) (2022) 185–189.
[10] J. Zeng, M. Lu, H. Liu, et al., Realistic flat-band model based on degenerate p-orbitals in two-dimensional ionic materials, Sci. Bull. 66 (8) (2021) 765–770.
[11] B. Cui, X. Zheng, J. Wang, et al., Realization of Lieb lattice in covalent-organic frameworks with tunable topology and magnetism, Nat. Commun. 11 (1) (2020) 1–8.
[12] W. Jiang, H. Huang, F. Liu, A Lieb-like lattice in a covalent-organic framework and its Stoner ferromagnetism, Nat. Commun. 10 (1) (2019) 1–7.
[13] S. Li, Y. Xie, Y. Chen, Isolated flat bands in a lattice of interlocking circles, Phys. Rev. B 104 (8) (2021) 085127.
[14] E. Tang, J.-W. Mei, X.-G. Wen, High-temperature fractional quantum Hall states, Phys. Rev. Lett. 106 (23) (2011) 236802.
[15] S.D. Huber, E. Altman, Bose condensation in flat bands, Phys. Rev. B 82 (18) (2010) 184502.
[16] C. Wu, D. Bergman, L. Balents, et al., Flat bands and Wigner crystallization in the honeycomb optical lattice, Phys. Rev. Lett. 99 (7) (2007) 070401.
[17] Y. Chen, S. Xu, Y. Xie, et al., Ferromagnetism and Wigner crystallization in Kagome graphene and related structures, Phys. Rev. B 98 (3) (2018) 035135.
[18] S. Peotta, P. Törmä, Superfluidity in topologically nontrivial flat bands, Nat. Commun. 6 (1) (2015) 1–9.
[19] H. Tasaki, Ferromagnetism in the Hubbard models with degenerate single-electron ground states, Phys. Rev. Lett. 69 (10) (1992) 1608.
[20] B. Huang, G. Clark, E. Navarro-Moratalla, et al., Layer-dependent ferromagnetism in a van der Waals crystal down to the monolayer limit, Nature 546 (7657) (2017) 270–273.
[21] M.A. McGuire, G. Clark, K. Santosh, et al., Magnetic behavior and spin-lattice coupling in cleavable van der Waals layered $CrCl_3$ crystals, Phys. Rev. Mater. 1 (1) (2017) 014001.
[22] D.A. Broadway, S.C. Scholten, C. Tan, et al., Imaging domain reversal in an ultrathin van der Waals ferromagnet, Adv. Mater. 32 (39) (2020) 2003314.
[23] X.-W. Shen, W.-Y. Tong, S.-J. Gong, et al., Electrically tunable polarizer based on 2D orthorhombic ferrovalley materials, 2D Mater. 5 (1) (2017) 011001.
[24] K. Lee, A.H. Dismukes, E.J. Telford, et al., Magnetic order and symmetry in the 2D semiconductor CrSBr, Nano Lett. 21 (8) (2021) 3511–3517.
[25] X. Jiang, Q. Liu, J. Xing, et al., Recent progress on 2D magnets: Fundamental mechanism, structural design and modification, Appl. Phys. Rev. 8 (3) (2021) 031305.
[26] X. Li, J. Yang, First-principles design of spintronics materials, Natl. Sci. Rev. 3 (3) (2016) 365–381.
[27] Z. Wang, T. Zhang, M. Ding, et al., Electric-field control of magnetism in a few-layered van der Waals ferromagnetic semiconductor, Nat. Nanotechnol. 13 (7) (2018) 554–559.
[28] T. Song, X. Cai, M.W.-Y. Tu, et al., Giant tunneling magnetoresistance in spin-filter van der Waals heterostructures, Science 360 (6394) (2018) 1214–1218.
[29] C. Cardoso, D. Soriano, N. García-Martínez, et al., Van der Waals spin valves, Phys. Rev. Lett. 121 (6) (2018) 067701.
[30] D. Zhong, K.L. Seyler, X. Linpeng, et al., Van der Waals engineering of ferromagnetic semiconductor heterostructures for spin and valleytronics, Sci. Adv. 3 (5) (2017) e1603113.
[31] M. Maksymenko, A. Honecker, R. Moessner, et al., Flat-band ferromagnetism as a Pauli-correlated percolation problem, Phys. Rev. Lett. 109 (9) (2012) 096404.
[32] E. Bobrow, J. Zhang, Y. Li, Ferromagnetic percolation transition in a multiorbital flat band assisted by Hund's coupling, Phys. Rev. B 104 (6) (2021) 064442.
[33] D. Green, L. Santos, C. Chamon, Isolated flat bands and spin-1 conical bands in two-dimensional lattices, Phys. Rev. B 82 (7) (2010) 075104.
[34] Y. Hwang, J.-W. Rhim, B.-J. Yang, General construction of flat bands with and without band crossings based on wave function singularity, Phys. Rev. B 104 (8) (2021) 085144.
[35] J. Wang, S.Y. Quek, Isolated flat bands and physics of mixed dimensions in a 2D covalent organic framework, Nanoscale 12 (39) (2020) 20279–20286.
[36] M.S. de Sousa, F. Liu, F. Qu, et al., Vacancy-engineered flat-band superconductivity in holey graphene, Phys. Rev. B 105 (1) (2022) 014511.
[37] Y. Yang, Z. Tang, B. Zhou, et al., In situ no-slot joint integration of half-metallic $C(CN)_3$ cocatalyst into g-C_3N_4 scaffold: An absolute metal-free in-plane heterosystem for efficient and selective photoconversion of CO_2 into CO, Appl. Catal. B Environ. 264 (2020) 118470.
[38] L. Liu, X. Wu, X. Liu, et al., Electronic structure and magnetism in g-C_4N_3 controlled by strain engineering, Appl. Phys. Lett. 106 (13) (2015) 132406.
[39] A. Du, S. Sanvito, S.C. Smith, First-principles prediction of metal-free magnetism and intrinsic half-metallicity in graphitic carbon nitride, Phys. Rev. Lett. 108 (19) (2012) 197207.
[40] A. Bafekry, M. Neek-Amal, F. Peeters, Two-dimensional graphitic carbon nitrides: Strain-tunable ferromagnetic ordering, Phys. Rev. B 101 (16) (2020) 165407.
[41] A. Bafekry, S.F. Shayesteh, F.M. Peeters, Two-dimensional carbon nitride (2DCN) nanosheets: Tuning of novel electronic and magnetic properties by hydrogenation, atom substitution and defect engineering, J. Appl. Phys. 126 (21) (2019) 215104.
[42] A. Bafekry, M. Faraji, M. Fadlallah, et al., Two-dimensional porous graphitic carbon nitride C_6N_7 monolayer: First-principles calculations, Appl. Phys. Lett. 119 (14) (2021) 142102.
[43] A. Bafekry, M. Faraji, N. Hieu, et al., Two-dimensional Dirac half-metal in porous carbon nitride C_6N_7 monolayer via atomic doping, Nanotechnology 33 (7) (2021) 075707.
[44] G. Zhou, Y. Shan, Y. Hu, et al., Half-metallic carbon nitride nanosheets with micro grid mode resonance structure for efficient photocatalytic hydrogen evolution, Nat. Commun. 9 (1) (2018) 1–9.
[45] J.S. Lee, X. Wang, H. Luo, et al., Fluidic carbon precursors for formation of functional carbon under ambient pressure based on ionic liquids, Adv. Mater. 22 (9) (2010) 1004–1007.
[46] X. Shi, C. He, C.J. Pickard, et al., Stochastic generation of complex crystal structures combining group and graph theory with application to carbon, Phys. Rev. B 97 (1) (2018) 014104.
[47] C. He, X. Shi, S.J. Clark, et al., Complex low energy tetrahedral polymorphs of group IV elements from first principles, Phys. Rev. Lett. 121 (17) (2018) 175701.
[48] X. Shi, J. Li, T. Ouyang, et al., New structure candidates for the experimentally synthesized heptazine-based and triazine-based two dimensional graphitic carbon nitride, Physica E 128 (2021) 114535.
[49] G. Kresse, J. Furthmüller, Efficient iterative schemes for ab initio total-energy calculations using a plane-wave basis set, Phys. Rev. B 54 (16) (1996) 11169.
[50] R. Pons, A. Mielke, T. Stauber, Flat-band ferromagnetism in twisted bilayer graphene, Phys. Rev. B 102 (23) (2020) 235101.
[51] G. Bouzerar, Flat band induced room-temperature ferromagnetism in two-dimensional systems, Phys. Rev. B 107 (18) (2023) 184441.
[52] R. Resta, Macroscopic polarization in crystalline dielectrics: The geometric phase approach, Rev. Mod. Phys. 66 (3) (1994) 899.
[53] S.N. Shirodkar, U.V. Waghmare, Emergence of ferroelectricity at a metal-semiconductor transition in a 1T monolayer of MoS_2, Phys. Rev. Lett. 112 (15) (2014) 157601.
[54] L. Li, M. Wu, Binary compound bilayer and multilayer with vertical polarizations: Two-dimensional ferroelectrics, multiferroics, and nanogenerators, ACS Nano 11 (6) (2017) 6382–6388.
[55] G. Henkelman, H. Jónsson, Improved tangent estimate in the nudged elastic band

method for finding minimum energy paths and saddle points, J. Chem. Phys. 113 (22) (2000) 9978–9985.
[56] K.-A.N. Duerloo, M.T. Ong, E.J. Reed, Intrinsic piezoelectricity in two-dimensional materials, J. Phys. Chem. Lett. 3 (19) (2012) 2871–2876.
[57] R. Bistritzer, A.H. MacDonald, Moiré bands in twisted double-layer graphene, Proc. Natl Acad. Sci. 108 (30) (2011) 12233–12237.
[58] G. Tarnopolsky, A.J. Kruchkov, A. Vishwanath, Origin of magic angles in twisted bilayer graphene, Phys. Rev. Lett. 122 (10) (2019) 106405.
[59] T. Sarkar, D. Wei, J. Zhang, et al., Ferromagnetic order beyond the superconducting dome in a cuprate superconductor, Science 368 (6490) (2020) 532–534.
[60] C. Tschirhart, M. Serlin, H. Polshyn, et al., Imaging orbital ferromagnetism in a moiré Chern insulator, Science 372 (6548) (2021) 1323–1327.

Author profile

Chaoyu He is a fully professor in School of Physics and Optoelectronics in XiangTan University since 2022. He got his B.S. and Ph.D. degrees from Xiangtan University in 2009 and 2015, respectively. His research interest includes computational condensed mater physics and computational materials science, including crystal structure prediction and functional materials design. He has developed the Random method combined with Group and Graph theory (RG2) for crystal structures prediction (www.crystal-rg2.cn) and discovered numerous novel material structures and physical phenomena. He was awarded Science Fund for Distinguished Young Scholars of Hunan Province of China (No. 2021JJ10036) in 2021.

Tao Ouyang is a fully professor in School of Physics and Optoelectronics in Xiangtan University since 2023. He got his B.S. and Ph.D. degrees from Xiangtan University in 2007 and 2012, respectively. He has been persistently performing research on the core topic of thermal and thermoelectric transport properties in micronanostructures. Up to now, he has published more than 60 papers as first author or corresponding author in the mainstream international academic journals. He was awarded the youth science and technology talent project of Hunan Province (Grant No. 2022RC1197) in 2021 and won the third prize of the 2020 Hunan Provincial Natural Science Award (the first completed person).

Huimin Zhang currently is working as a postdoctoral researcher in Key Laboratory of Quantum Materials and Devices of Ministry of Education, School of Physics in Southeast University. She got her Ph. D degree in physics from school of physics, Southeast University in 2020. Then she worked as a postdoctoral researcher in Department of Physics, Fudan University during 2020.05–2022.11. Her research interests are ferroelectric, magnetic, and multiferroic materials.

Hongjun Xiang is a full professor at Physics Department in Fudan University since 2009. He got his B.S. (in 2001) and Ph.D. (in 2006) degrees from University of Science and Technology of China. From 2006 to 2009, he worked as a postdoc in North Carolina State University and National Renewable Energy Laboratory. Prof. Xiang focuses on the research in the field of computational condensed matter physics, and has done leading works in the establishment of theoretical models of quantum materials and development of new methods. The main achievements include: (1) He proposed a unified model of spin-order induced ferroelectricity and a four-state method to calculate the strength of magnetic interactions and magnetoelectric couplings. (2) He developed a software package, namely, PASP (Property Analysis and Simulation Package for materials) that integrates several methods for material simulation and design. He was awarded the National Science Fund for Distinguished Young Scholars from NSFC and the ICTP prize from International Centre for Theoretical Physics in 2018, and the Huang Kun Physics Award from the Chinese Physical Society in 2023. He was elected as APS Fellow in 2021.